Article

Research on a Variable-Leakage-Flux Permanent Magnet Motor Control System Based on an Adaptive Tracking Estimator

Xiaolei Cai [1], **Qixuan Wang** [1], **Yucheng Wang** [2] **and Li Zhang** [1,*]

1   School of Electrical and Information Engineering, Jiangsu University, Zhenjiang 212013, China
2   State Grid Zhenjiang Power Supply Company, Zhenjiang 212013, China
*   Correspondence: jennyzhang@ujs.edu.cn; Tel.: +86-0511-88791245

Abstract: Due to the characteristics of inductance parameter mismatch and back electromotive force harmonics caused by novel leakage flux branches and other non-ideal factors for the variable-leakage-flux permanent magnet (VLF-PM) motor, its control system suffers from a deteriorated performance of the rotor position estimation. To overcome the problems mentioned above, an adaptive tracking estimator of the rotor position is proposed in this paper for the VLF-PM motor control system. First, the proposed method simplifies the VLF-PM motor mathematical model and reduces the effect of inductance parameter variations according to the active flux concept. Then, robust and gradient descent algorithms are utilized to maintain the robustness of inductance parameter variations and eliminate the specific order harmonics owing to the novel leakage flux branches. Meanwhile, the accuracy and stability are enhanced. Furthermore, the position compensation based on the current adaptive tracking strategy is proposed to compensate the rotor position error caused by other non-ideal factors. Finally, the feasibility of the proposed estimated system is verified.

1. Introduction

Owing to the advantages of high power density, compact structure, high efficiency and energy saving properties, the permanent magnet synchronous motor (PMSM) has been widely used in electric vehicles (EVs) [1]. A wide speed range and high efficiency under a wide area of its drive motor are required to meet the multiple operating conditions of EVs [2]. However, the traditional PMSM has a shortcoming in that the speed regulation range is limited due to the constant PM magnetic field. In contrast to the traditional PMSM, the variable-leakage-flux permanent magnet (VLF-PM) motor has variable salient characteristics, which can meet the requirements of EVs with variable operating conditions and a wide speed range [3].

For a VLF-PM motor control system, the acquisition of the high-precision rotor position is very important. Sensorless control is a good way to overcome the above problems, which has become an important research direction in the field of motor control [4,5]. Typically, sensorless control technology can be divided into the high-frequency signal injection method, based on the motor's salient characteristics, and the method based on the back-EMF model. For the former method, additional energy loss, torque ripple and high-frequency noise will be caused because of the injection voltage signal. In addition, the application speed range is limited to zero/low speed [6]. Therefore, the back-EMF based sensorless control model at medium/high speed is usually used to obtain rotor position information, such as the sliding mode observer (SMO) method [7], extended Kalman filter method [8], model reference adaptive method [9], etc. Among the above sensorless control methods, the SMO has the advantages of strong robustness and simple structure, and has therefore been widely used.

Since the VLF-PM motor contains a variation of magnetic flux, it has the characteristics of parameter variations. Aiming at the motor parameters' variations of sensorless control, relevant research on the real-time acquisition of motor parameters has been carried out [10–13]. The parameter identification methods obtain the real-time parameters of the motor online, which can modify the control model in real-time through the identified parameters. Thus, high-performance control can be achieved. In [11], a high-frequency square wave excitation signal was injected to extract the current response to identify inductance. This method is simple to extract signals and can achieve inductance identification with the consideration of the saturation effect. However, due to the need for continuous excitation signals, the voltage utilization will be reduced. To achieve online parameter identification and feed back into the back-EMF model, an improved SMO was proposed in [12]. Nevertheless, this algorithm only can identify a single parameter of stator resistance online, which is not applicable to the sensorless control of the VLF-PM motor with multi-parameter changes.

Apart from the motor parameter variations of the VLF-PM motor, it also has abundant magnetic field space harmonics because of the special magnetic circuit design. Correspondingly, specific subharmonics in the back-EMF will be caused, which brings great challenges for sensorless control of the VLF-PM motor. For harmonic suppression, the existing research has mainly focused on optimizing the motor's magnetic circuit design and the control algorithm [14]. Compared with the harmonic suppression methods from motor structure optimization, the optimization methods from a control algorithm can suppress harmonics without changing the existing hardware conditions. In [15], a synchronous frequency rotation filter was used to directly extract the fundamental back-EMF, which can simplify the control algorithm. However, the existence of a low-pass filter will lead to the degradation of the dynamic performance of the motor drive system. Thus, a bilinear recursive least squares adaptive filter was proposed in [16], which can effectively track the back-EMF and filter out the specified harmonic components. Nevertheless, due to the use of recursive least squares, the control system is too complex and unstable.

In summary, lots of research has been conducted on the sensorless control of variable parameters and multi-harmonic motors [17–20]. However, the above studies were not suitable for the sensorless control of the VLF-PM motor with large parameter variations and specific subharmonics. Motivated by this, a new adaptive tracking estimator-based sensorless control method is proposed in this paper, which can effectively overcome the problems of parameter variations and specific harmonic back-EMF. This paper is organized as follows. The VLF-PM motor structure, parameter characteristics and sensorless control based on the conventional SMO method are introduced in Section 2. In Section 3, a new adaptive tracking estimator based on the SMO is presented. First, the proposed method simplified the model for the sensorless control system, and it reduced the effect of inductance parameter variations according to the concept of the effective flux model. Then, the gradient descent algorithm was utilized to eliminate the specific order harmonics caused by the novel leakage flux branches, and maintain robustness against the inductance parameter variations. Meanwhile, the position compensation based on the current adaptive tracking strategy is proposed in this section, which suppressed the estimated position error influenced by other non-ideal factors. Furthermore, the experimental results are presented to validate the proposed sensorless control strategy for the VLF-PM motor in Section 4, and the accuracy and stability of the proposed system are verified by comparison. Finally, the main contents of the proposed estimated system are summarized, and the key conclusions are drawn in Section 5.

2. Machine Description and Its Sensorless Control

2.1. Machine Description

The structure and corresponding design concept of the VLF-PM motor are shown in Figure 1. It can be known that an elliptical magnetic barrier and one layer of arc-shaped magnetic barriers are set along the *q*-axis magnetic field. This makes all *q*-axis magnetic

flux pass through the magnetic bridge. Thus, the *q*-axis magnetic flux and the PM leakage flux are converged at the magnetic bridge and influenced by each other. Consequently, the *q*-axis magnetic flux can be changed by controlling the *q*-axis current, which can realize the control of the saturation degree in the flux leakage magnetic bridge. Owing to these magnetic flux variation characteristics, the VLF-PM motor can possess an obvious speed extension effect.
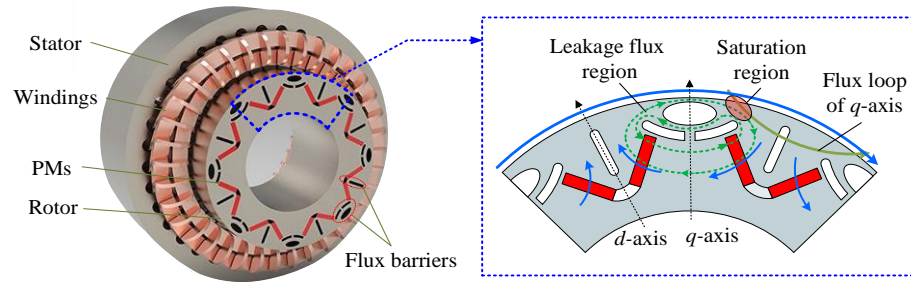

Figure 1. Configuration of VLF-PM motor.

The inductance characteristics of L_d and L_q of the VLF-PM motor are shown in Figure 2. It can be seen that both L_d and L_q of the VLF-PM motor are affected by the *q*-axis current. Figure 3 shows the no-load back-EMF and harmonic analysis of the VLF-PM motor. It can be seen that the stator current of the VLF-PM motor contains specific subharmonics. In addition, the back-EMF contains $6K \pm 1$ harmonic because of the inverter nonlinearity [16]. Furthermore, the relevant parameters of the VLF-PM motor are listed in Table 1.
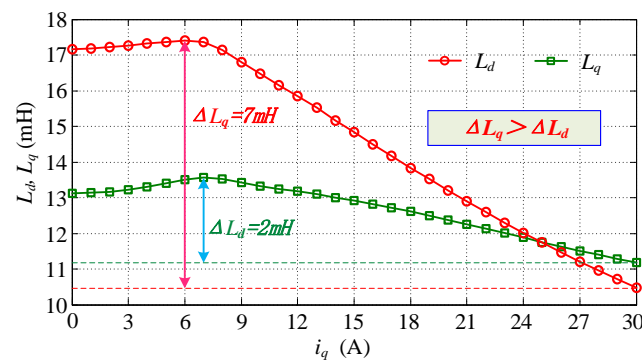

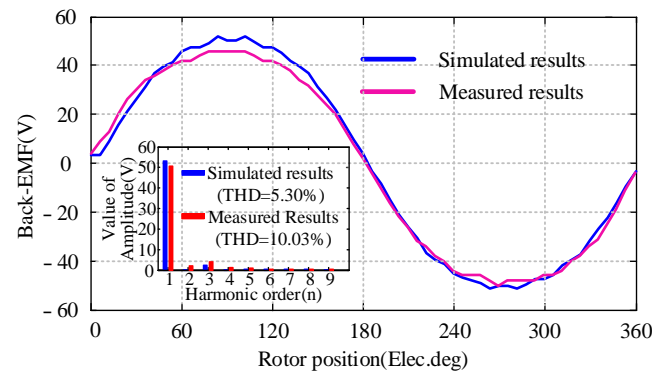**Figure 2.** Relationship between inductances and *q*-axis current.

Figure 3. No-load back-EMF and its harmonics analysis.

Table 1. Parameters of the VLF-PM motor.

Parameter	Value	Parameter	Value
Rated power	3.5 kW	Stator resistance	0.29 Ω
Rated phase current	20 A	Rated torque	28 N·m
Number of rotor pole-pairs	4	Rated speed	1200 r/min

2.2. Sensorless Control Based on SMO

Based on [21–23], the observer is constructed according to the asymmetric voltage model, which is shown in Figure 4. Since the back-EMF contains rotor position information, the SMO can be constructed by using the switching function to make it equivalent to the extended back-EMF, which is expressed as follows.

$$p \begin{bmatrix} \tilde{i}_\alpha \\ \tilde{i}_\beta \end{bmatrix} = \frac{1}{L_d} \begin{bmatrix} -R & -\omega_e(L_d - L_q) \\ \omega_e(L_d - L_q) & -R \end{bmatrix} \begin{bmatrix} \tilde{i}_\alpha \\ \tilde{i}_\beta \end{bmatrix} + \frac{1}{L_d} \begin{bmatrix} e_\alpha - \hat{e}_\alpha \\ e_\beta - \hat{e}_\beta \end{bmatrix} \tag{1}$$

where the superscript "~" indicates the error between the actual and estimated value; R is the stator resistance; L_d and L_q are the stator inductance in the d-q axis, respectively; ω_e is the rotor angular velocity; ψ_{PM} is the PM flux linkage; p is the differential operator; e_α and e_β are the extended back-EMFs; θ_e is the rotor position electrical angle.
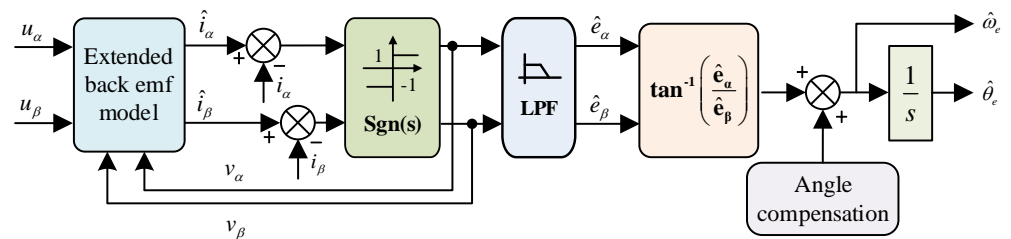
Figure 4. Block diagram of the SMO based on the extended back-EMF.

The sliding mode control rate is designed as:

$$\begin{bmatrix} \hat{e}_\alpha \\ \hat{e}_\beta \end{bmatrix} = \begin{bmatrix} k\mathrm{sgn}(\hat{i}_\alpha - i_\alpha) \\ k\mathrm{sgn}(\hat{i}_\beta - i_\beta) \end{bmatrix} \tag{2}$$

where the superscript "^" indicates the estimated value, $k > \{\max|e_\alpha|, |e_\beta|\}$.

By using the arctangent function, the estimated rotor position can be expressed as:

$$\hat{\theta}_e = -\arctan(\hat{e}_\alpha / \hat{e}_\beta) \tag{3}$$

where $\hat{\theta}_e$ is the estimated rotor position electrical angle and $\hat{e}_\alpha$ and $\hat{e}_\beta$ are the estimated extended back-EMFs.

2.3. Analysis of Position Accuracy

Due to the special design of the VLF-PM motor, its dynamic and steady-state performances are different when compared with the conventional PM motor. For the VLF-PM motor drive system with a conventional sensorless control strategy, there are key problems as [24]:

(1)   Variation of the motor parameters

From the inductance characteristics of the VLF-PM motor, as shown in Figure 2, it can be known that the q-axis current has little influence on L_d, but a great influence on L_q. Thus, the extended back-EMF can be rewritten as:

$$\hat{E}' = \hat{E} + j\hat{\omega}_e \Delta L_q \hat{i}_s \tag{4}$$

where $\hat{E}$ and $\hat{E}'$ are the estimated back-EMFs before and after the change of motor parameters, respectively.

From (4), the influence of an inductance mismatch on the estimated back-EMF can be obtained as shown in Figure 5. It can be noted that the amplitude and phase of the estimated back–EMF will be affected by the inductance mismatch whether the motor operates at $i_d = 0$ or $i_d \neq 0$. Consequently, the variable parameter characteristics of the VLF-PM motor will deteriorate the observed accuracy of the sensorless control based on the extended back-EMF.
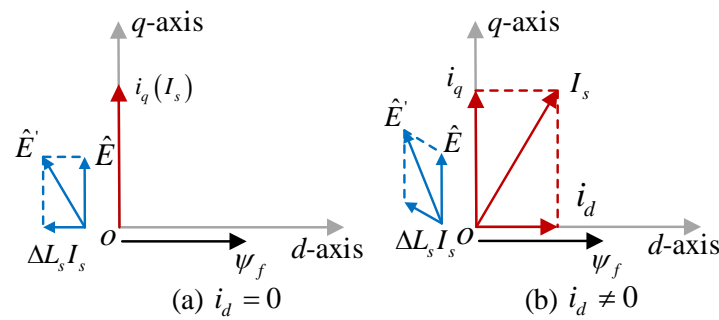

Figure 5. Influence of inductance mismatch on the estimated back-EMF.

(2)   Harmonics in the back-EMF

As previously analyzed, the back-EMF of the VLF-PM motor contains specific harmonics. With the consideration of the harmonics, the phase current can be expressed as:

$$i_n = I_1 \sin\left(\omega_e t + \varphi_1 - i \cdot \frac{2}{3}\pi\right) + \sum_{k=2} I_k \sin\left(k\omega_e t + \varphi_k - i \cdot \frac{2}{3}\pi\right) \tag{5}$$

where n represents any phase of a, b and c; I_1 and I_k are the amplitude of the fundamental and harmonic wave, respectively; φ_1 and φ_k are the initial phases of the fundamental and harmonic wave, respectively.

With the coordinate transformation, the back-EMFs in the α-β axis are obtained as:

$$e_\alpha = (L_d - L_q)\omega_e \begin{cases} \left[\dfrac{\psi_{PM}}{(L_d - L_q)} + I_1 \sin(\varphi_1)\right](-\sin(\omega_e t)) \\ + \sum_{k=1}^{n} \frac{k \pm 1}{2} I_k[\cos((k \pm 1)\omega_e t + \varphi_{k \pm 1})] \\ - \sum_{k=1}^{n} \frac{k \mp 1}{2} I_k[\cos((k \mp 1)\omega_e t - \varphi_{k \mp 1})] \end{cases} \tag{6}$$

$$e_\beta = (L_d - L_q)\omega_e \begin{cases} \left[\dfrac{\psi_{PM}}{(L_d - L_q)} + I_1 \sin(\varphi_1)\right]\cos(\omega_e t) \\ + \sum_{k=1}^{n} \frac{k \pm 1}{2} I_k[\sin((k \pm 1)\omega_e t + \varphi_{k \pm 1})] \\ - \sum_{k=1}^{n} \frac{k \mp 1}{2} I_k[\sin((k \mp 1)\omega_e t - \varphi_{k \mp 1})] \end{cases} \tag{7}$$

From the above analysis it can be known that due to the harmonic components, the estimated accuracy of sensorless control will be greatly deteriorated. To reduce the influence of spatial harmonic signals on the control system, gradient descent algorithms are introduced to suppress the harmonics. The specific methods will be described in detail in Section 3.

(3)　Other non-ideal factors

When the vector control strategy with the "$i_d = 0$" control is adopted, the electromagnetic torque of the VLF-PM motor is expressed as:

$$T_e = \frac{3}{2} P_n i_q \psi_{\text{pm}} \tag{8}$$

Due to the estimated position error in sensorless control, there is a corresponding deviation between the actual and estimated currents. Thus, the torque with a rotor position error can be expressed as:

$$T_e = \frac{3}{2} P_n \psi_{\text{pm}} |i_s| \cos \Delta\theta_{error} \tag{9}$$

The relationship between the current vector and the estimated position error under the "$i_d = 0$" control is shown in Figure 6. It can be seen that since the "$i_d = 0$" control is adopted, i_s is all provided by i_d. Therefore, if there is no deviation in the estimated rotor position, that is, when $\Delta\theta_{error} = 0$, the projection of current in the d-axis direction is 0. Then, the amplitude of i_s is the non-minimum and only part of the current is used to generate torque.
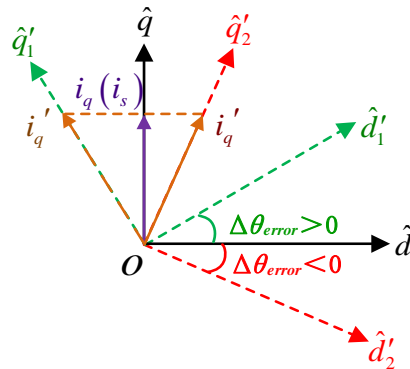

Figure 6. Relationship between the current vector and the estimated position error.

From the above analysis, with the adoption of the "$i_d = 0$" control, the estimated position error can be considered as the minimum when the amplitude of i_s is the minimum. Therefore, it is necessary to design an adaptive position compensation with a goal of the minimal amplitude of i_s. For the VLF-PM motor, by detecting the amplitude of i_s, the estimated position errors caused by the inductance variations and other non-ideal factors can be compensated.

3. New SMO Based on an Adaptive Tracking Estimator

To overcome the above-mentioned problems, a new SMO based on an adaptive tracking estimator is proposed in this paper.

3.1. Design of the New SMO

Since the magnetic circuit of the dq-axis of the interior PMSM is asymmetric, the inductance matrix based on the extended back-EMF will contain a coupling term related to the motor's saliency. However, due to the variable salient characteristics of the VLF-PM motor, its extended back-EMF method will face more complex coupling. Therefore, an effective flux model is introduced in this paper to decouple the coupling terms in the model related to inductances and to simplify the model for the sensorless control system [25].

The effective back-EMF can be decoupled into fundamental and harmonic components, which are represented as:

$$e = e_f + e_h \tag{10}$$

Based on the idea of the effective flux model, the current state equation under the α–β axis can be rewritten as:

$$pi_{\alpha\beta} = -\frac{R}{L_q}i_{\alpha\beta} + \frac{1}{L_q}u_{\alpha\beta} - \frac{1}{L_q}e_{f\alpha\beta} - \frac{1}{L_q}e_{h\alpha\beta} \tag{11}$$

From (11), it can be known that the effective flux model can eliminate the coupling term of $(L_d - L_q)$, and the changes of R and L_d have little influence on the estimated position error [26]. However, L_q will still affect the accuracy of sensorless control under different operating conditions.

To improve the robustness of the change of L_q, the new SMO is designed as:

$$p\hat{i}_{\alpha\beta} = -\frac{R}{L_q}\hat{i}_{\alpha\beta} + \frac{1}{L_q}u_{\alpha\beta} - \frac{1}{L_q}\left[\frac{\kappa\sigma_{\alpha\beta}}{|\sigma_{\alpha\beta}| + \delta_{\alpha\beta}} + x^n(w^n)^T\right] \tag{12}$$

where the superscript "^" indicates the observed quantity, κ is the observer gain, $\sigma_{\alpha\beta}$ is the introduced variable and $\delta_{\alpha\beta}$ is the positive constant.

Assume that the fundamental component of the effective back-EMF is:

$$e_f = \frac{\kappa\sigma_{\alpha\beta}}{|\sigma_{\alpha\beta}| + \delta_{\alpha\beta}} \tag{13}$$

with

$$\sigma_{\alpha\beta} = \kappa\frac{\widetilde{i}_{\alpha\beta}}{L_q} \tag{14}$$

In addition, the harmonic component of the effective back-EMF is assumed as

$$e_h^n = \sum_{i=0}^{k} x^n(w^n)^T \tag{15}$$

where x^n is the reference input vector and k is the harmonic frequency. Furthermore, x^n can be expressed as

$$x^n = \begin{bmatrix} \cos(k\omega_e t) & \sin(k\omega_e t) \end{bmatrix} \tag{16}$$

where w^n is the adjustable weight factor, which can be expressed as

$$w^n = \begin{bmatrix} w_{\cos}^n & w_{\sin}^n \end{bmatrix} \tag{17}$$

where $w_{\cos}^n$ and $w_{\sin}^n$ are the two components of the weight factors of x^n, respectively. They are used to adjust the respective components to achieve the minimum value.

Based on the idea of convex optimization in neural networks [27], the gradient descent optimization (GDO) algorithm is introduced into the sensorless control system in this paper to suppress the harmonics. The weight factor can change adaptively with the output vector and finally the input vector can reach the expected value. In our research, the regulation and selection of the weight factors are performed to achieve the minimal harmonic component of the effective back-EMF.

To achieve the above purpose, the weight factor w^n is adapted to the speed to achieve the minimal error between $x^n(w^n)^T$ and the harmonic component of the back-EMF, which can decouple the harmonic component. Thus, the complexity of the algorithm can be effectively reduced while the accuracy of the estimation is guaranteed. The structure of the GDO algorithm is shown in Figure 7.
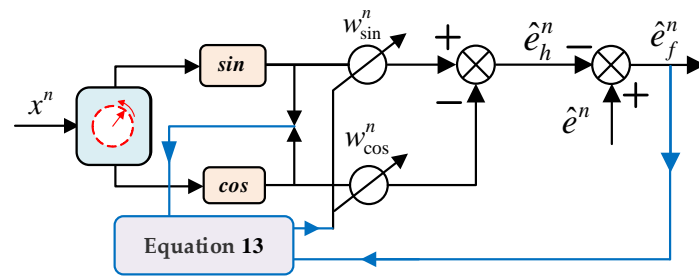
Figure 7. Structure of the GDO.

Take the difference between the total effective back-EMF and the harmonic component of the effective back-EMF, which is expressed as

$$\Lambda^n = \hat{e}_f^n == \hat{e}^n - \hat{e}_h^n = \hat{e}^n - x^n(w^n)^T \tag{18}$$

According to the GDO algorithm, the difference between the total effective back-EMF and the harmonic component of the effective back-EMF can be minimized. From (10), it can be known that when the error in (18) reaches the minimum, the harmonic component reaches the maximum value because the total back-EMF is unchanged. Then, it can be ascertained that when the difference between the total back-EMF and the harmonic component reaches the maximum value, the harmonic component in the total back-EMF can be considered to be suppressed. Hence, the harmonic component is decoupled.

From the above analysis, it can be known that the purpose of decoupling can be achieved when (18) is finally close to the fundamental component of the effective back-EMF. To eliminate the harmonic component adaptively, the weight factor should be modified continuously according to the speed. Therefore, to obtain the updated expression of the weight factor, let the evaluation function be:

$$J^n(w^n) = \frac{1}{2}(\Lambda^n)^2 = \frac{1}{2}\left(\hat{e}^n - x^n(w^n)^T\right)^2 \tag{19}$$

To minimize the value of the above evaluation function, it is necessary to update it iteratively along the negative direction of the gradient of the evaluation function. In this case, the value of the evaluation function will decrease with the updated weight factor and finally converge. Take the gradient of the evaluation function concerning the weight factor as

$$\nabla J^n(w^n) = -\left(\hat{e}^n - x^n(w^n)^T\right)x^n = -\Lambda^n x^n \tag{20}$$

According to (20), the updated function of the weight factor can be denoted as $w^n(k)$, which is expressed as

$$w^n(k+1) = w^n(k) - \eta \nabla J^n(w^n) = w^n(k) + \eta \Lambda^n(k)x^n(k) \tag{21}$$

where η is the step factor or learning rate.

Taking the difference between (11) and (12), the error equation of the current can be obtained as

$$p\widetilde{i}_{\alpha\beta} = -\frac{R}{L_q}\widetilde{i}_{\alpha\beta} + \frac{1}{L_q}e_{f\alpha\beta} + \frac{1}{L_q}e_{h\alpha\beta} - \frac{1}{L_q}\left[\frac{\kappa\sigma_{\alpha\beta}}{|\sigma_{\alpha\beta}| + \delta_{\alpha\beta}} + x^n(w^n)^T\right] \tag{22}$$

where the superscript "~" represents the error.

When the estimated current error converges to zero, the fundamental component of the back-EMF can be expressed as

$$\hat{e}_{f\alpha\beta} = \frac{\kappa\sigma_{\alpha\beta}}{|\sigma_{\alpha\beta}| + \delta_{\alpha\beta}} \tag{23}$$

Finally, the rotor position information by orthogonal phase-locked loop can be obtained as

$$\varepsilon = \frac{1}{\sqrt{\hat{e}_{f\alpha}^2 + \hat{e}_{f\beta}^2}} \left[\hat{e}_{f\alpha} \cos \hat{\theta}_e - \hat{e}_{f\beta} \sin \hat{\theta}_e \right] \tag{24}$$

$$\hat{\theta}_e = (1/s)(k_i/s + k_p)\varepsilon \tag{25}$$

It should be noted that to improve the estimated accuracy of the rotor position, normalization processing is adopted in this paper.

According to Lyapunov stability [28,29], the stability of the designed observer can be obtained and the current error will gradually converge to zero. In addition, the proposed observer has good robustness against the inductance parameter variations.

3.2. Position Compensation Based on the Current Adaptive Tracking Strategy

To suppress the estimated position error influenced by other non-ideal factors, the position compensation based on the current adaptive tracking strategy is proposed in this paper.

Generally, if the current fluctuation is large, the current difference between adjacent sampling points will be distorted. Hence, a moving average filter (MAF) is adopted to smooth the sampled current signals, which can make the current difference more accurate and improve the performance of the position compensation algorithm [30]. The MAF in the continuous domain is expressed as

$$\overline{x}(t) = \frac{1}{T_w} \int_{t-T_w}^{t} x(\tau) d\tau \tag{26}$$

where $x(\tau)$ is the current signal containing clutter, T_w is the window length of MAF and $\overline{x}(t)$ is the filtered signal.

Based on (26), the frequency domain transfer function of MAF can be deduced as

$$G_{MAF}(s) = \frac{\overline{x}(s)}{x(s)} = \frac{1 - e^{-T_w s}}{T_w s} \tag{27}$$

Furthermore, the MAF amplitude frequency is expressed as

$$G_{MAF}(jw) = \left| \frac{\sin(\omega T_w/2)}{\omega T_w/2} \right| \angle -\omega T_w/2 \tag{28}$$

According to the first-order Pade approximation, when T_w is small, the MAF expression can be approximately equivalent to the first-order inertia link, which is shown as follows:

$$G_{MAF}(s)\Big|_{e^{-T_w s} \approx \frac{1-T_w s/2}{1+T_w s/2}} \approx \frac{1}{T_w s/2 + 1} \tag{29}$$

The MAF in the discrete domain is expressed as:

$$\overline{x}(k) = \frac{1}{N} \sum_{i=0}^{N} x(k-i) \tag{30}$$

From the above equation, the differential expression of MAF is:

$$\overline{X}(z) = \frac{1}{N} \frac{1 - z^{-N}}{1 - z^{-1}} X(z) \tag{31}$$

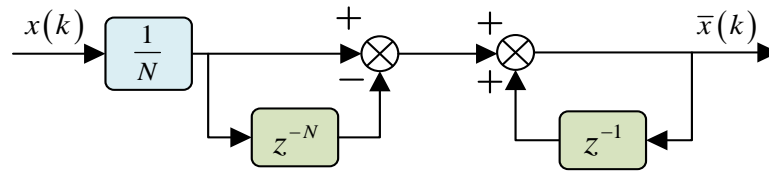A block diagram of MAF is presented in Figure 8.

Figure 8. Block diagram of MAF.

To make the current vector adaptively track the minimum value and compensate the position estimation error caused by the change of inductance parameters and other non-ideal factors, the position compensation algorithm based on adaptive current tracking is adopted in this paper. The flow chart of adaptive current tracking compensation is shown in Figure 9, where dq_{comp} is the adjustment step of this position compensation algorithm, Δq_{error} is the estimated rotor position error and k is the execution period of this algorithm.
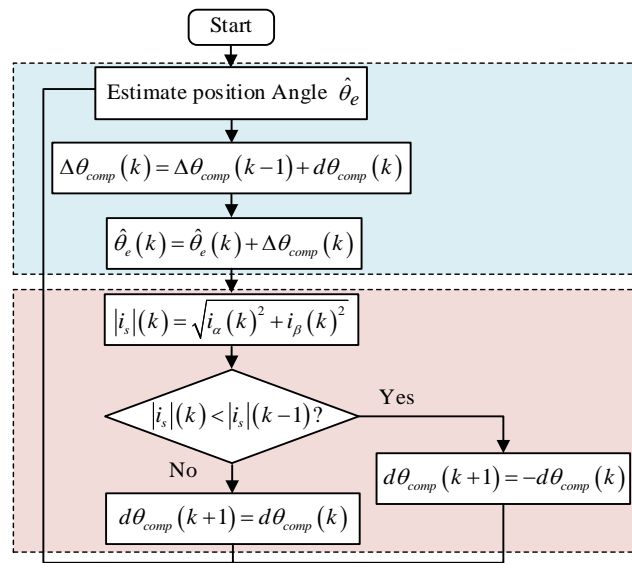

Figure 9. Flowchart of the adaptive current tracking compensation strategy.

Firstly, the initial value and direction of the step size $d\theta_{comp}$ are set, and the changes of the current at time k and time $(k − 1)$ are compared. If $i(k)$ is less than $i(k − 1)$, the compensation direction of $d\theta_{comp}$ is correct, and the compensation direction of $d\theta_{comp}$ in the next period will be unchanged. If $i(k)$ is greater than $i(k − 1)$, the compensation direction of $d\theta_{comp}$ is incorrect, which will result in an increase in the current compared with the previous time. Then, the compensation direction of $d\theta_{comp}$ in the next cycle should be changed. By detecting the change of current at time k and $(k − 1)$, the compensation direction of the next cycle $d\theta_{comp}$ can be adjusted. Correspondingly, the compensation angle can be adaptively adjusted, which finally converges to the minimum value. So, the compensation of the position estimation error can be achieved, and the final compensation angle can be expressed as:

$$\Delta\theta_{comp} = \sum_{k=1}^{+\infty} d\theta_{comp} \tag{32}$$

From (32), it can be known that the compensation speed of the position estimation error depends on the adjustment step size $d\theta_{comp}$ and the execution period k of the algorithm. If $d\theta_{comp}$ increases, the compensation speed will be faster, but the chattering of the position compensation angle will be larger. If $d\theta_{comp}$ decreases, the compensation speed will slow down, and the chattering will decrease.

Based on the new SMO and position compensation, the proposed SMO-based adaptive tracking estimator is constructed; its block diagram is shown in Figure 10.
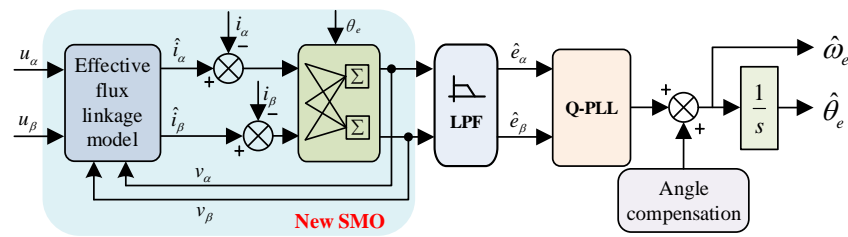
Figure 10. Block diagram of new SMO based on an adaptive tracking estimator.

3.3. Proposed VLF-PM Motor Control System

Figure 11 gives the proposed sensorless control system of the VLF-PM motor based on an adaptive tracking estimator.
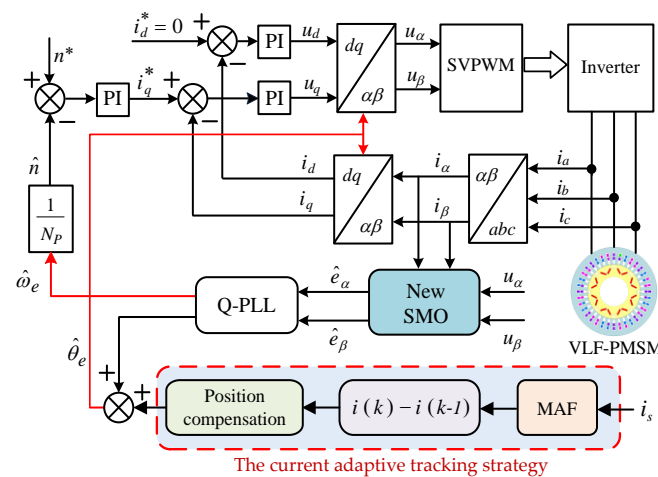

Figure 11. Block diagram of the proposed VLF-PM motor control system based on an adaptive tracking estimator.

From Figure 11, it can be seen that with a new SMO, the back-EMF can be observed. In addition, the harmonic components of the back-EMF can be decoupled. Then, the rotor position signal can be obtained with the PLL. Thus, it can improve the observation accuracy and reduce the harmonic fluctuation error. Furthermore, with the current adaptive tracking strategy, the position estimation error caused by the inductance variations and other non-ideal factors can be adaptively compensated. According to the above analysis of a proposed VLF-PM motor control system, it can be concluded that with the proposed estimator in this paper, the estimated accuracy of the rotor position of the VLF-PM motor control system can be greatly improved.

4. Verification Results

Figure 12 shows the experimental platform of the proposed VLF-PM motor control system. The proposed sensorless control strategy is implemented on the controller of a dSPACE DS1007.

To verify the effectiveness of the proposed method, the steady-state performance of the sensorless control method based on the traditional and new SMO is compared. Figure 13 shows the experimental waveforms of the traditional SMO method at a speed of 200 r/min and a load of 20 N·m. It can be observed that when the parameters of the VLF-PM motor change, the rotor position error will be larger. Additionally, the traditional method has more harmonic content of the back-EMF, which leads to the oscillation of the estimated speed and rotor position. Thus, it can be ascertained that the estimated error of the traditional SMO of the VLF-PM motor control is large. Moreover, due to the special design of the VLF-PM motor design, space harmonics are brought into the magnetic flux.

Correspondingly, there are some distortions in the back-EMF and obvious oscillations in the speed and rotor position error, which brings great challenges to the reliability and comfort of EVs.
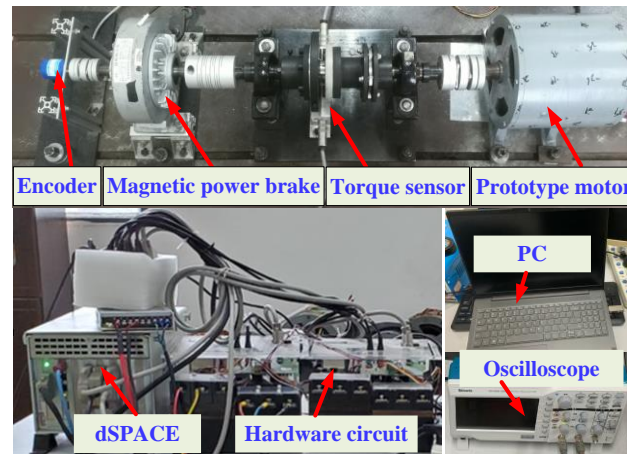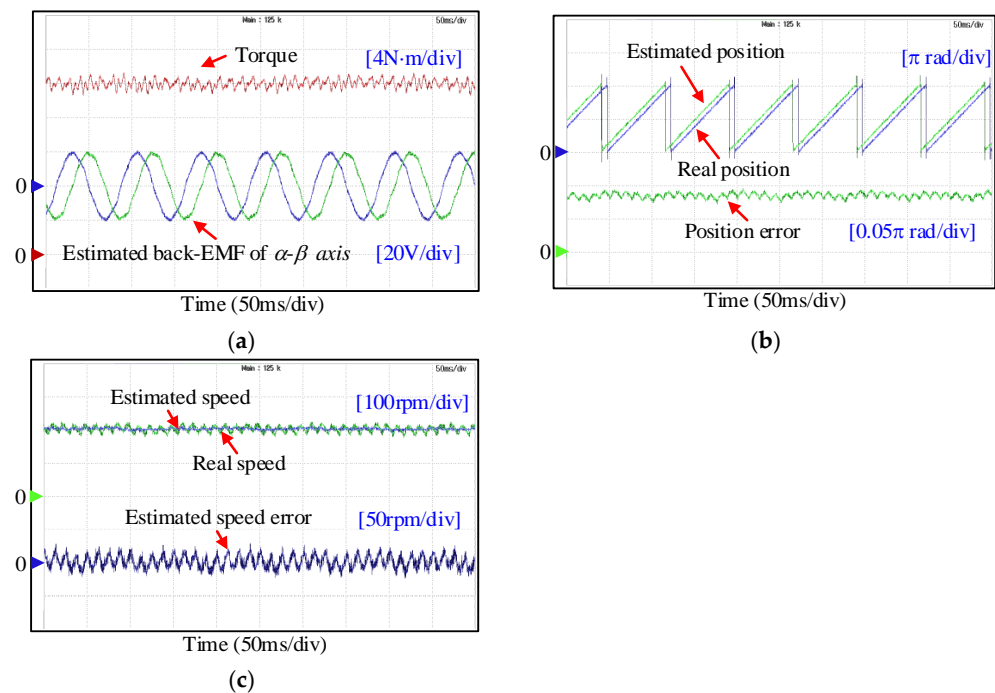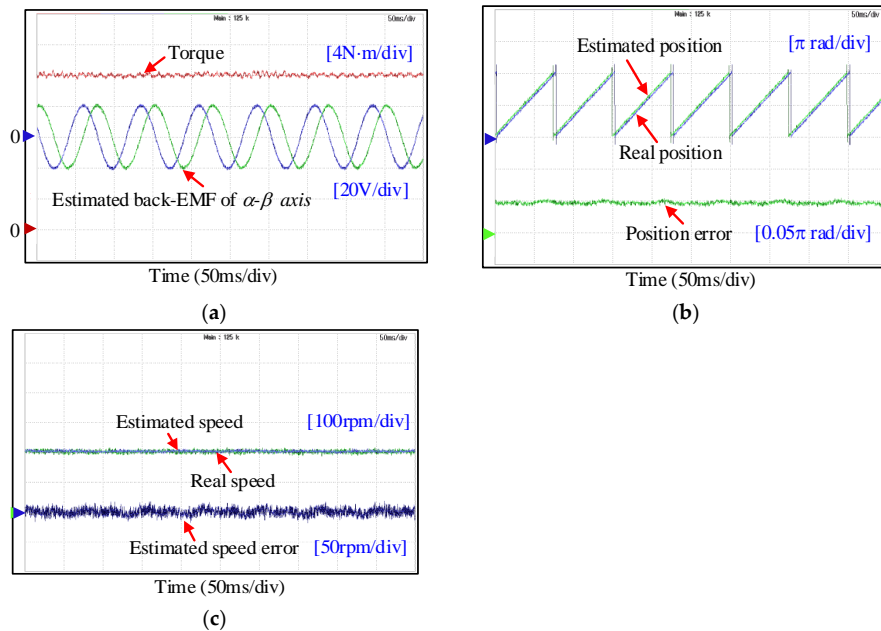

Figure 12. Experimental platform.

Figure 13. Steady-state performance of the conventional SMO. (**a**) Estimated back-EMF and torque; (**b**) real position, estimated position and position error; (**c**) real speed, estimated speed and estimated speed error.

Figure 14 shows the steady-state experimental waveform of the sensorless control system based on the proposed method. Compared with the traditional SMO, it can be found that the maximum rotor error, the oscillation and the oscillation of the speed error are all decreased significantly. It can be concluded that the proposed VLF-PM motor control system can well suppress the specific subharmonics in the back-EMF. Thus, the oscillation of the speed and rotor position, and the rotor position estimation error can be reduced. Furthermore, an FFT analysis of the harmonic components of the back-EMF of the traditional method and the proposed method are shown in Figure 15. It can be known that due to the special rotor structure design of the VLF-PM motor, the back-EMF is

distorted, which leads to obvious oscillations in the estimated speed and position errors. In contrast, the proposed method can effectively suppress the second, fourth, fifth and seventh harmonics. Furthermore, the back-EMF waveform can be successfully corrected, which demonstrates that the periodic pulsation in the estimated speed and position error can be suppressed.

(a)

(b)

(c)

Figure 14. Steady-state performance of the new SMO. (**a**) Estimated back-EMF and torque; (**b**) real position, estimated position and position error; (**c**) real speed, estimated speed and estimated speed error.

(a)

(b)
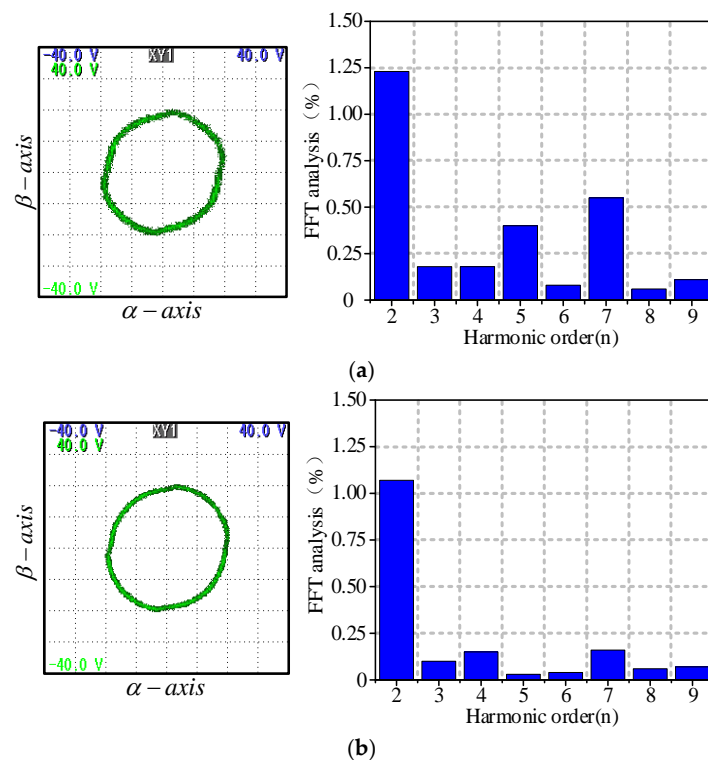
Figure 15. FFT analysis of the estimated back-EMF. (**a**) Results of the traditional SMO. (**b**) Results of the proposed method.

Figure 16 shows the effect comparison before and after the estimated position error compensation based on the current adaptive tracking strategy.
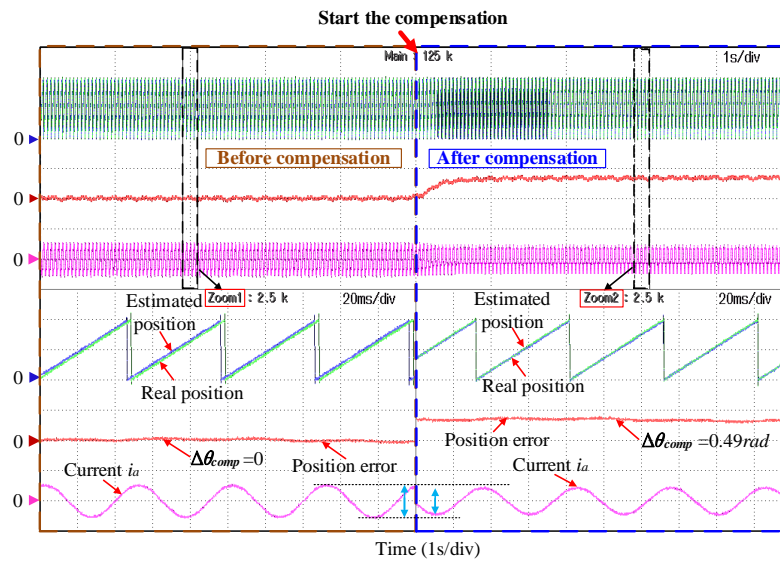

Figure 16. Results of rotor position error compensation based on the adaptive current tracking strategy.

It was found that within 0.5 s after the compensation algorithm is cut in, the adaptive angle compensation can be carried out according to the magnitude of the current vector. Aiming at minimizing the current amplitude, the estimated position error is compensated adaptively. The current amplitude can be reduced markedly, compared with that before compensation. In addition, compared with before compensation, the difference between the actual and estimated rotor position is also reduced, indicating that the proposed method can compensate for the rotor position estimation error caused by motor parameter changes and other non-ideal factors.

Furthermore, the dynamic estimation performance of the traditional method and the proposed method at a speed of 600 r/min are compared in Figure 17a,b. With the varied inductance parameter of the VLF-PM motor under the changed operating conditions, the rotor position error is only about 0.05 π rad and maintains a small change. In addition, it was found that the estimated speed and rotor position of the proposed method can still follow the actual value well, even with the variated operating conditions, which can possess good robustness against the inductance parameter variations. Therefore, it can be concluded that the proposed method can improve both steady-state and dynamic performance, which further verifies the effectiveness of the proposed scheme.
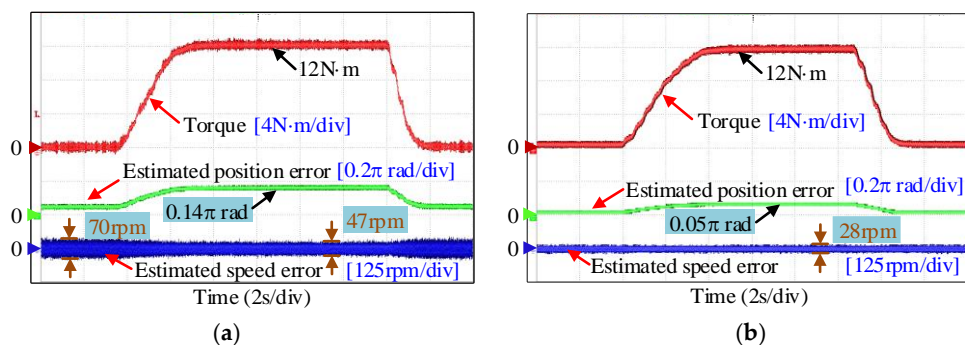

Figure 17. Dynamic performance of the sensorless control system. (**a**) Results of the traditional SMO. (**b**) Results of the proposed method.

5. Conclusions

Based on the analysis of the variable leakage characteristics of the VLF-PM motor, a new SMO based on an adaptive tracking estimator has been developed to overcome the issues related to the reduced rotor position estimation accuracy of sensorless control systems. The following advantages of the proposed control strategy were ascertained:

(1) The effective flux model is used to eliminate the coupling term of $(L_d - L_q)$ and reduce the influence of multiple inductance parameter changes on the system. Thus, the problems of decreased estimation accuracy and the oscillation of the estimated value, caused by the change of multiple inductance parameters and the estimated back-EMF harmonics, have been solved.

(2) A gradient descent algorithm was introduced to design the position observer, which improved the robustness of the proposed observer against the variation of the inductance parameters of the VLF-PM motor. At the same time, the specific harmonic in the VLF-PM motor was further suppressed to reduce its influence on the control system. Hence, the observation accuracy of the sensorless control for the VLF-PM motor has been effectively improved.

(3) The position compensation based on the current adaptive tracking strategy was proposed to compensate the rotor position error caused by other non-ideal factors. The accurate rotor position signals were obtained by the online compensation of the initial estimated rotor position. Furthermore, the online compensation of the rotor position offset error was achieved. Therefore, the estimation performance of the sensorless control system for the VLF-PM motor has been improved.

As the experimental results showed, the proposed method solved the problems caused by the variation of inductance parameters and the spatial harmonics of the VLF-PM motor sensorless drive system under different working conditions. The proposed motor sensorless drive system has a good steady-state and dynamic performance, which could meet the stability and comfort requirements of EVs. Furthermore, the research has a certain reference value for the study of sensorless control of motors with large parameter variations or specific subharmonics.

Author Contributions: Conceptualization, L.Z.; methodology, X.C.; software, Q.W. and Y.W.; validation, X.C., Q.W. and Y.W.; formal analysis, X.C.; investigation, X.C. and Q.W.; resources, Y.W.; data curation, X.C.; writing—original draft preparation, L.Z. and X.C.; writing—review and editing, Q.W., Y.W. and X.C.; project administration, L.Z.; funding acquisition, L.Z. All authors have read and agreed to the published version of the manuscript.

Conflicts of Interest: The authors declare no conflict of interest.

References

1. Zhang, Y.; Zhao, C.; Dai, B.; Li, Z. Dynamic Simulation of Permanent Magnet Synchronous Motor (PMSM) Electric Vehicle Based on Simulink. *Energies* **2022**, *15*, 1134. [CrossRef]
2. Zhang, L.; Zhu, X.Y.; Xu, L.; Zhang, C.; Fan, Y. Simplified Universal Fault-Tolerant Direct Torque Control of FPFTPM Motor with Steady-Healthy Design under Open-Circuit Fault. *IEEE Trans. Ind. Electron.* **2022**, *69*, 6688–6699. [CrossRef]
3. Fukushige, T.; Limsuwan, N.; Kato, T.; Akatsu, K.; Lorenz, R.D. Efficiency contours and loss minimization over a driving cycle of a variable flux-intensifying machine. In Proceedings of the 2013 IEEE Energy Conversion Congress and Exposition, Denver, CO, USA, 15–19 September 2013; pp. 591–597. [CrossRef]
4. Dianov, A.; Anuchin, A. Adaptive Maximum Torque per Ampere Control of Sensorless Permanent Magnet Motor Drives. *Energies* **2020**, *13*, 5071. [CrossRef]
5. Qian, L.; Sun, L.; Wang, K.; Tong, M. Fusion of Position Estimation Techniques for a Swing Servo by Permanent Magnet Synchronous Machine. *IEEE Trans. Ind. Electron.* 2022, *Early Access*. [CrossRef]
6. Wang, S.; Zhao, J.; Yang, K. High Frequency Square-Wave Voltage Injection Scheme-Based Position Sensorless Control of IPMSM in the Low- and Zero- Speed Range. *Energies* **2019**, *12*, 4776. [CrossRef]

7.　Qiao, Z.; Shi, T.; Wang, Y.; Yan, Y.; Xia, C.; He, X. New Sliding-Mode Observer for Position Sensorless Control of Permanent-Magnet Synchronous Motor. *IEEE Trans. Ind. Electron.* **2013**, *60*, 710–719. [CrossRef]

8.　Pasqualotto, D.; Rigon, S.; Zigliotto, M. Sensorless Speed Control of Synchronous Reluctance Motor Drives Based on Extended Kalman Filter and Neural Magnetic Model. *IEEE Trans. Ind. Electron.* **2023**, *70*, 1321–1330. [CrossRef]

9.　Nguyen, T.; Rafaq, M.S.; Choi, H.H.; Jung, J.W. A Model Reference Adaptive Control Based Speed Controller for a Surface-Mounted Permanent Magnet Synchronous Motor Drive. *IEEE Trans. Ind. Electron.* **2018**, *65*, 9399–9409. [CrossRef]

10.　Hang, J.; Ding, S.; Ren, X.; Sun, W.; Hu, Q.; Huang, Y.; Hua, W.; Wang, Q. Integration of Inter-Turn Fault Diagnosis and Fault-Tolerant Control for Direct-Torque-Controlled PMSM Drive System. *IEEE Trans. Power Electron.* **2021**, *36*, 11124–11134. [CrossRef]

11.　Wu, X.; Zhu, Z.Q.; Freire, N.M.A. High Frequency Signal Injection Sensorless Control of Finite-Control-Set Model Predictive Control With Deadbeat Solution. In Proceedings of the 2021 IEEE Energy Conversion Congress and Exposition (ECCE), Vancouver, BC, Canada, 10–14 October 2021; pp. 4698–4703. [CrossRef]

12.　Liang, D.; Li, J.; Qu, R. Sensorless control of permanent magnet synchronous machine based on second-order sliding-mode observer with online resistance estimation. *IEEE Trans. Ind. Electron.* **2017**, *53*, 3672–3682. [CrossRef]

13.　Morimoto, S.; Sanada, M.; Takeda, Y. Mechanical sensorless drives of IPMSM with online parameter identification. *IEEE Trans. Ind. Electron.* **2006**, *42*, 1241–1248. [CrossRef]

14.　Zhang, S.; Zheng, P.; Jahns, T.M.; Cheng, L.; Wang, M.; Sui, Y. A novel variable-flux permanent-magnet synchronous machine with quasi-series magnet configuration and passive flux barrier. In Proceedings of the 2018 IEEE International Magnetics Conference (INTERMAG), Singapore, 23–27 April 2018; p. 1. [CrossRef]

15.　Li, Z.; Wang, X.; Huang, G.; Wan, H.; Chen, Y. Ripple Analysis and Suppression Method Research of Direct Drive Permanent Magnet Synchronous Wind Turbine under Wind Shear. *Energies* **2020**, *13*, 5088. [CrossRef]

16.　Wu, X.; Huang, S.; Liu, K.; Lu, K.Y.; Hu, Y.S.; Pan, W.L.; Peng, X.Y. Enhanced Position Sensorless Control Using Bilinear Recursive Least Squares Adaptive Filter for Interior Permanent Magnet Synchronous Motor. *IEEE Trans. Power Electron.* **2020**, *35*, 681–698. [CrossRef]

17.　Kesavan, P.; Karthikeyan, A. Electromagnetic Torque-Based Model Reference Adaptive System Speed Estimator for Sensorless Surface Mount Permanent Magnet Synchronous Motor Drive. *IEEE Trans. Ind. Electron.* **2020**, *67*, 5936–5947.

18.　Zhang, X.G.; Bai, H.L.; Cheng, M. Improved Model Predictive Current Control with Series Structure for PMSM Drives. *IEEE Trans. Ind. Electron.* **2022**, *69*, 12437–12446. [CrossRef]

19.　Wang, F.; Li, J.; Li, Z.; Ke, D.; Du, J.; Garcia, C.; Rodriguez, J. Design of Model Predictive Control Weighting Factors for PMSM Using Gaussian Distribution-Based Particle Swarm Optimization. *IEEE Trans. Ind. Electron.* **2022**, *69*, 10935–10946. [CrossRef]

20.　Zhang, L.; Bai, J.; Wu, J. Speed Sensor-Less Control System of Surface-Mounted Permanent Magnet Synchronous Motor Based on Adaptive Feedback Gain Supertwisting Sliding Mode Observer. *J. Sens.* **2021**, *2021*, 8301359. [CrossRef]

21.　Mobayen, S.; Mostafavi, S.; Fekih, A. Non-Singular Fast Terminal Sliding Mode Control with Disturbance Observer for Underactuated Robotic Manipulators. *IEEE Access* **2020**, *8*, 198067–198077. [CrossRef]

22.　Repecho, V.; Waqar, J.B.; Biel, D.; Doria-Cerezo, A. Zero Speed Sensorless Scheme for Permanent Magnet Synchronous Machine Under Decoupled Sliding-Mode Control. *IEEE Trans. Ind. Electron.* **2021**, *69*, 1288–1297. [CrossRef]

23.　Liu, Y.; Fang, J.; Tan, K.; Huang, B.; He, W. Sliding mode observer with adaptive parameter estimation for sensorless control of IPMSM. *Energies* **2020**, *13*, 5991. [CrossRef]

24.　Tsai, W.C.; Wu, C.H.; Cheng, M.Y. Tracking accuracy improvement based on adaptive nonlinear sliding mode control. *IEEE/ASME Trans. Mechatron.* **2021**, *26*, 179–190. [CrossRef]

25.　Lin, Q.; Liu, L.; Liang, D. Hybrid Active Flux Observer to Suppress Position Estimation Error for Sensorless IPMSM Drives. *IEEE Trans. Power Electron.* **2023**, *38*, 872–886. [CrossRef]

26.　Diao, N.; Zhang, Y.; Sun, X.; Song, C.; Wang, W.; Zhang, H. A Real-Time Open-Circuit Fault Diagnosis Method Based on Hybrid Model Flux Observer for Voltage Source Inverter Fed Sensorless Vector Controlled Drives. *IEEE Trans. Power Electron.* **2023**, *38*, 2539–2551. [CrossRef]

27.　El-Sousy, F.F.M.; Amin, M.M.; Mohammed, O.A. Robust Adaptive Neural Network Tracking Control With Optimized Super-Twisting Sliding-Mode Technique for Induction Motor Drive System. *IEEE Trans. Ind. Electron.* **2022**, *58*, 4134–4157. [CrossRef]

28.　Zhang, Q.; Fan, Y. The Online Parameter Identification Method of Permanent Magnet Synchronous Machine under Low-Speed Region Considering the Inverter Nonlinearity. *Energies* **2022**, *15*, 4314. [CrossRef]

29.　Mfoumboulou, Y.D.; Mnguni, M.E.S. Development of a New Linearizing Controller Using Lyapunov Stability Theory and Model Reference Control. *Indones. J. Electr. Eng. Comput. Sci.* **2022**, *25*, 1328–1343. [CrossRef]

30.　Li, H.; Zhang, X.; Xu, C.; Hong, J. Sensorless Control of IPMSM Using Moving-Average-Filter Based PLL on HF Pulsating Signal Injection Method. *IEEE Trans. Energy Convers.* **2020**, *35*, 43–52. [CrossRef]